# **NJC**



View Article Online **PAPER** 

Synthesis of SiO<sub>2</sub>@MnCo<sub>2</sub>O<sub>4</sub> core-shell

nanorattles using layered double hydroxide

precursors and studies on their peroxidase-like



Cite this: New J. Chem., 2023, 47, 3266

> activity† Pankaj Rana and Pethaiyan Jeevanandam \*\*

Received 5th October 2022, Accepted 9th January 2023

DOI: 10.1039/d2nj04901e

rsc.li/njc

The current work demonstrates a simple soft chemical approach to synthesize SiO<sub>2</sub>@MnCo<sub>2</sub>O<sub>4</sub> coreshell nanorattles using SiO<sub>2</sub>@MnCo-LDH (layered double hydroxide) precursors. XRD analysis indicates the formation of MnCo<sub>2</sub>O<sub>4</sub> nanoparticles (NPs) on SiO<sub>2</sub> spheres. FESEM images show hierarchical flower-like MnCo<sub>2</sub>O<sub>4</sub> NPs on the surface of the SiO<sub>2</sub> spheres. TEM micrographs show the interstitial space between the core (SiO<sub>2</sub>) and the shell (MnCo<sub>2</sub>O<sub>4</sub>), indicating the core-shell nanorattle morphology of SiO<sub>2</sub>@MnCo<sub>2</sub>O<sub>4</sub>. BET adsorption-desorption isotherms of the SiO<sub>2</sub>@MnCo<sub>2</sub>O<sub>4</sub> core-shell nanorattles indicate their mesoporous nature with high surface area. Optical studies indicate  $O^{2-} \rightarrow Mn^{2+}$  and  $O^{2-} \rightarrow Co^{3+}$  charge-transfer transitions and d-d transition in pure MnCo<sub>2</sub>O<sub>4</sub> NPs and the SiO<sub>2</sub>@Mn- $Co_2O_4$  core-shell nanorattles. XPS measurements indicate the presence of Si<sup>4+</sup>, Mn<sup>2+</sup>, Co<sup>2+</sup>, Mn<sup>3+</sup>,  $Co^{3+}$ , and  $O^{2-}$  in the  $SiO_2@MnCo_2O_4$  core—shell nanorattles. The  $SiO_2@MnCo_2O_4$  core—shell nanorattles show paramagnetic and superparamagnetic behavior at 300 K and 5 K, respectively. After characterization, the SiO<sub>2</sub>@MnCo<sub>2</sub>O<sub>4</sub> core-shell nanorattles were explored for peroxidase-like activity for the first time. The SiO<sub>2</sub>@MnCo<sub>2</sub>O<sub>4</sub> core-shell nanorattles act as a peroxidase nanozyme and exhibit better peroxidase-like activity than pure MnCo<sub>2</sub>O<sub>4</sub> NPs and horseradish peroxidase.

## Introduction

Recently, core-shell NPs have received considerable attention due to their remarkable properties. Combining two different materials (core and shell) changes the properties of the original core and the shell.<sup>1</sup> Among core-shell NPs, core-shell nanorattles or yolk-shell nanoparticles possess interesting morphological features. Core-shell nanorattles or yolk-shell nanostructures have advantages because of their core@void@shell configuration. Core-shell nanorattles possess enhanced properties due to the void space between the core and the shell.<sup>1,2</sup> Core-shell nanorattles based on metal oxides have several promising applications such as in drug delivery, catalysis, sensing, Li-ion batteries, and adsorption.<sup>2,3</sup> Lee et al. have reported Au@SiO2 yolk-shell structures as catalyst for the reduction of p-nitrophenol.4 Kandula et al. have reported peroxidase-like activity of SiO<sub>2</sub>@Co<sub>3</sub>O<sub>4</sub> nanorattles.<sup>5</sup> Chen et al. have reported lithium storage properties of α-Fe<sub>2</sub>O<sub>3</sub>@SnO<sub>2</sub> nanorattles. Rokicinska et al. have reported Co<sub>3</sub>O<sub>4</sub>@SiO<sub>2</sub>

Department of Chemistry, Indian Institute of Technology Roorkee, Roorkee-247667, India. E-mail: jeevafcy@iitr.ac.in; Fax: +91-1332-273560; Tel: +91-1332-285444 † Electronic supplementary information (ESI) available. See DOI: https://doi.org/ 10.1039/d2nj04901e

core-shell nanorattles for catalytic combustion of toluene. Hu et al. have reported α-Fe<sub>2</sub>O<sub>3</sub>@SiO<sub>2</sub> and SnO<sub>2</sub>@SiO<sub>2</sub> coreshell nanorattles as anticancer drug carriers.8

Silica (SiO<sub>2</sub>) is an amorphous insulator, which is stable at high temperatures and in water. The spherical morphology and porous nature of SiO<sub>2</sub> make it a good candidate as a core material for the synthesis of silica-based core-shell NPs/nanorattles.9 SiO2-based nanorattles have been studied for various applications such as Co@SiO<sub>2</sub> core-shell nanorattles as catalysts, <sup>10</sup> α-Fe<sub>2</sub>O<sub>3</sub>@SiO<sub>2</sub> and SnO<sub>2</sub>@SiO<sub>2</sub> core-shell nanorattles as anticancer drug carriers,<sup>8</sup> SiO<sub>2</sub>@Co<sub>3</sub>O<sub>4</sub> core-shell nanorattles as nanozymes,<sup>5</sup> rattle-type gold nanorods/SiO<sub>2</sub> nanocomposites for chemo-photothermal therapy, 11 Au@SiO2 yolk-shell nanostructures as catalyst for reduction of p-nitrophenol, and Fe<sup>0</sup> asiO<sub>2</sub> nanoparticles as catalyst for Fentonlike reaction.12

MnCo<sub>2</sub>O<sub>4</sub> is a spinel-type metal oxide in which Mn<sup>2+</sup> ions occupy octahedral (Oh) sites, and Co2+ and Co3+ ions occupy both tetrahedral (T<sub>d</sub>) and O<sub>h</sub> sites. 13 Due to the high oxidation potential of cobalt and high electron transport ability of manganese, MnCo2O4 exhibits exceptional electrochemical and physicochemical properties. 14 MnCo2O4 nanoparticles are used in diverse applications such as asymmetric supercapacitors, anode materials in Li-ion batteries, photocatalysis, adsorption, and oxygen reduction. 14-18 MnCo<sub>2</sub>O<sub>4</sub>-based core-shell NPs have

**Paper** NJC

been used in different applications. For example, Wang et al. have reported MnCo2O4@MnCo2S4 core-shell nanostructures for asymmetric supercapacitors.<sup>19</sup> Zhao et al. have reported MnCo<sub>2</sub>O<sub>4</sub>(a)Ni(OH)<sub>2</sub> core-shell flowers with ultrahigh specific capacitance.<sup>20</sup> Li et al. have reported MnCo<sub>2</sub>O<sub>4</sub>@NiCo<sub>2</sub>O<sub>4</sub> coreshell NPs for dye-sensitized solar cells.21 Sun et al. have reported MnCo<sub>2</sub>O<sub>4</sub>@C core-shell nanowires for water splitting.<sup>22</sup> Zhao et al. have reported Co<sub>3</sub>O<sub>4</sub>(a)MnCo<sub>2</sub>O<sub>4</sub> core-shell nanowire arrays for electrochemical energy storage.<sup>23</sup> Mehrez et al. have reported MnCo<sub>2</sub>O<sub>4</sub>@NiMoO<sub>4</sub> core-shell nanowire arrays for supercapacitor applications.24

Enzymes are biocatalysts that catalyze several biochemical reactions with high efficiency and selectivity. 25 Natural enzymes have several limitations. They have low stability, complex storage requirements, high cost, and less adaptability under harsh environmental conditions.<sup>26</sup> To overcome the drawbacks of natural enzymes, nanomaterials have been used as an alternative. Metal oxide-based nanozymes have been explored to mimic different natural enzymes such as peroxidase, ferroxidase, catalase, and superoxide dismutase.26,27 Horseradish peroxidase oxidizes different substrates in the presence of hydrogen peroxide.<sup>28</sup> In the literature, different metal oxide-based nanozymes have been used as a peroxidase mimic. For example, Chen et al. have reported CuO nanoparticles for peroxidase-like activity.<sup>29</sup> Fu et al. have investigated the peroxidase-like activity of Fe<sub>3</sub>O<sub>4</sub> nanoparticles for cancer therapy. <sup>30</sup> Gao et al. have reported MnCo<sub>2</sub>O<sub>4</sub> nanofibers as a catalyst for peroxidase-like activity.<sup>31</sup> Ma et al. have reported photoinduced peroxidase-like activity of NiCo<sub>2</sub>O<sub>4</sub>@MnO<sub>2</sub> nanozymes.<sup>32</sup>

Multi-functional core-shell NPs and nanorattles have been synthesized using various soft chemical synthesis routes. For example, Wang et al. have reported the synthesis of MnCo<sub>2</sub>O<sub>4</sub>@MnCo<sub>2</sub>S<sub>4</sub> core-shell nanostructures using the hydrothermal method. 19 Zhao et al. have reported the synthesis of MnCo2O4@Ni(OH)2 core-shell flowers using homogeneous precipitation.<sup>20</sup> Mehrez et al. have reported the synthesis of MnCo2O4@NiMoO4 core-shell nanowires using hydrothermal method.24 Zhang et al. have reported the preparation of Co@CoO core-shell nanocomposites using solvothermal method.33 Gao et al. have reported the synthesis of NiCo2O4@SnO2 hetero-nanostructures using the hydrothermal method.<sup>34</sup> Kandula et al. have reported the preparation of SiO<sub>2</sub>(a) NiCo<sub>2</sub>O<sub>4</sub> core-shell nanorattles using homogeneous precipitation.<sup>35</sup>

The current work demonstrates a reliable and cost-effective synthetic strategy to prepare SiO2@MnCo2O4 nanorattles via calcination of SiO<sub>2</sub>@MnCo-LDH precursors at 500 °C. The MnCo<sub>2</sub>O<sub>4</sub> nanoparticles deposit on the surface of the SiO<sub>2</sub> spheres creating a hollow space (void) between the core and shell. The influence of [Mn<sup>2+</sup>:Co<sup>2+</sup>] ratio on the thickness of the MnCo<sub>2</sub>O<sub>4</sub> shell and void distance between the core (SiO<sub>2</sub>) and shell (MnCo<sub>2</sub>O<sub>4</sub>) has been investigated. The SiO<sub>2</sub>@MnCo<sub>2</sub>O<sub>4</sub> core-shell nanorattles exhibit better peroxidase-like activity than pure MnCo<sub>2</sub>O<sub>4</sub> NPs using 3,3',5,5'-tetramethylbenzidine (TMB) as the substrate. To the best of the authors' knowledge, there is no report on the synthesis of SiO<sub>2</sub>@MnCo<sub>2</sub>O<sub>4</sub> core-shell nanorattles and the SiO2@MnCo2O4 nanorattles have been employed as a peroxidase mimic for the first time.

## **Experimental**

## Reagents

Tetraethyl orthosilicate (98%, Sigma-Aldrich), ammonia solution (25%, Rankem), Mn(NO<sub>3</sub>)<sub>2</sub>.4H<sub>2</sub>O (97%, Sigma-Aldrich), Co(NO<sub>3</sub>)<sub>2</sub>.6H<sub>2</sub>O (98%, Merck), urea (99.5%, Rankem), 3,3',5,5'-tetramethylbenzidine (98%, Spectrochem Chemicals), ethanol (99.9%, Changshu Hongsheng Fine Chemical Co., Ltd.), and H<sub>2</sub>O<sub>2</sub> (30%, Rankem, AR). All the chemicals were used as received.

#### Synthesis of silica microspheres

SiO<sub>2</sub> microspheres were synthesized using a previously reported StÖber's method. 36 About 3.7 mL of tetraethyl orthosilicate was added (dropwise) to a mixture of 88 mL of EtOH and 12 mL of NH₄OH solution with constant stirring. The reaction mixture was continuously stirred at RT for 24 h to get a white-colored product. The product was centrifuged, washed with EtOH, and dried in an oven overnight at 70 °C.

#### Synthesis of SiO<sub>2</sub>@MnCo<sub>2</sub>O<sub>4</sub> core-shell nanorattles

First, SiO<sub>2</sub>@MnCo-LDH precursors were prepared using different molar ratios of [Mn2+: Co2+]. The synthetic parameters for the SiO<sub>2</sub>MnCo-LDH precursors are given in Table 1. In a typical synthetic experiment, Mn(NO<sub>3</sub>)<sub>2</sub>·4H<sub>2</sub>O, Co(NO<sub>3</sub>)<sub>2</sub>·6H<sub>2</sub>O and urea were dissolved in 100 mL of distilled water in a 250 mL beaker. Then, SiO2 microspheres (100 mg) were dispersed in the aqueous solution and sonicated for 10 minutes. The contents were heated at 85 °C for six hours with constant stirring. The product was collected by centrifuging and washing with deionized water and ethanol, followed by drying in an oven at 60 °C for about 12 h. The as-prepared SiO<sub>2</sub>@MnCo-LDH precursors were calcined at 500 °C (in a muffle furnace) for 3 h (heating rate = 2 °C per minute) in air to get the corresponding SiO<sub>2</sub>@MnCo<sub>2</sub>O<sub>4</sub> samples. The as-prepared SiO<sub>2</sub>@MnCo-LDH precursors, prepared using different molar ratios of [Mn<sup>2+</sup>:Co<sup>2+</sup>] (0.25:0.5, 0.5:1, and 1:2), will henceforth be referred to as SiO<sub>2</sub>@MnCo-LDH-0.25, SiO<sub>2</sub>@MnCo-LDH-0.5, and SiO<sub>2</sub>@MnCo-LDH-1, respectively. The SiO<sub>2</sub>@MnCo<sub>2</sub>O<sub>4</sub> samples, obtained on calcination, will henceforth be referred to as SiO<sub>2</sub>@MnCo<sub>2</sub>O<sub>4</sub>-0.25, SiO<sub>2</sub>@MnCo<sub>2</sub>O<sub>4</sub>-0.5, and SiO<sub>2</sub>@MnCo<sub>2</sub>O<sub>4</sub>-1, respectively.

#### Peroxidase-like activity and kinetic analysis

The peroxidase-like activity of the SiO2@MnCo2O4 nanorattles was studied utilizing tetramethylbenzidine (TMB) and H<sub>2</sub>O<sub>2</sub> as a substrate, and oxidizing agent, respectively. About 300 µL of 3 mM TMB solution (DMSO) and 31 µL of 100 mM H<sub>2</sub>O<sub>2</sub> were mixed with 3 mL of acetate buffer (0.1 M, pH = 5). Then, 30  $\mu$ L

Table 1 Synthetic details of SiO2@MnCo-LDH samples and their nomenclature

Sample code	[Mn <sup>2+</sup> ]:[Co <sup>2+</sup> ]			Temperature ( $^{\circ}$ C)	Time (h)
$\begin{array}{c} SiO_2@MnCo\text{-}LDH\text{-}0.25\\ SiO_2@MnCo\text{-}LDH\text{-}0.5 \end{array}$	0.5:1	100 100	1.0 1.0	85 85	6 6
SiO <sub>2</sub> @MnCo-LDH-1 MnCo-LDH	1:2 1:2	100 —	1.0 1.0	85 85	6 6

of catalyst dispersion (1 mg of SiO2@MnCo2O4 catalyst dispersed by sonication in 1 mL of deionized water) was added to the reaction mixture. The absorbance values (@ $\lambda_{max}$  = 652 nm) of the reaction mixture were measured using a UV-Vis spectrophotometer (Shimadzu UV-2600) up to 10 minutes. Kinetic experiments were performed by changing various experimental parameters, such as TMB concentration (0.05 to 0.5 mM), pH (2-12), catalyst dose (5–60  $\mu$ L), and H<sub>2</sub>O<sub>2</sub> concentration (5–200 mM). The kinetic parameters ( $K_{\rm m}$  and  $V_{\rm max}$ ) were estimated using the Michaelis-Menten equation and Lineweaver-Burk reciprocal plots.<sup>32</sup> The Michaelis-Menten equation is as follows.

$$1/V = (K_{\rm m}/V_{\rm max}) (1/[S]) + 1/V_{\rm max}$$

where  $K_{\rm m}$  and  $V_{\rm max}$  denote the Michaelis-Menten constant and maximum reaction velocity, respectively. V and [S] denote reaction velocity and concentration of the substrate (TMB), respectively.

Terephthalic acid was employed as a probe molecule to prove the role of hydroxyl radicals in the peroxidase-like activity of the SiO<sub>2</sub>@MnCo<sub>2</sub>O<sub>4</sub> nanorattles. In a cuvette, buffer (3 mL, pH = 5) and 100 mM  $H_2O_2$  (31  $\mu$ L) were mixed, followed by the addition of 30 µL of catalyst dispersion (SiO<sub>2</sub>@MnCo<sub>2</sub>O<sub>4</sub>). The reaction mixture was then treated with 0.5 mL of aqueous terephthalic acid solution (0.5 mM). A spectrofluorometer (Horiba Scientific, Fluoromax-4) was used to measure the PL spectra of the solution ( $\lambda_{exc}$  = 315 nm) up to 50 minutes.

#### Characterization

Powder X-ray diffraction patterns of all the samples were recorded using a Bruker AXS D8 Advance powder X-ray diffractometer (Cu-K<sub>x</sub>  $(\lambda = 1.5406 \text{ Å})$ , scan speed = 1° min<sup>-1</sup>) in the  $2\theta$  range of 5° to 90°. FT-IR spectra of the samples (using KBr pellets) were recorded using a Thermo Nicolet Nexus FT-IR spectrophotometer (4000 to 400 cm<sup>-1</sup>). A PerkinElmer Pyris Diamond instrument was used to perform thermal gravimetric analysis (TGA) of the SiO<sub>2</sub>@MnCo-LDH precursors; the precursors were heated at a rate of 10 °C min<sup>-1</sup> in air between 30 °C and 1000 °C. A Carl Zeiss Gemini scanning electron microscope (operating voltage = 20 kV) was used to examine the morphology of the samples. For elemental analysis, the SEM attached with an EDXA unit was employed. The core-shell nanorattles were imaged using an FEI Tecnai G2 20S-TWIN transmission electron microscope (operating voltage = 200 kV). Using a Quantum Design MPMS3 superconducting quantum interference device, the magnetic properties of the SiO<sub>2</sub>@MnCo<sub>2</sub>O<sub>4</sub> core-shell nanorattles were studied. X-ray photoelectron spectroscopy (XPS) measurements were performed on a Physical Electronics make (PHI 5000 Versa Probe III) spectrometer (Al- $K_{\alpha}$  radiation, energy = 1486.6 eV). Physisorption of N2 at 77 K was used to determine surface area of the SiO<sub>2</sub>(a)MnCo<sub>2</sub>O<sub>4</sub> core-shell nanorattles using a Quantachrome BET surface area analyzer (model = Nova 2200e).

## Results and discussion

The results related to SiO<sub>2</sub>@MnCo-LDH precursors are given in the ESI.† The results related to SiO<sub>2</sub>@MnCo<sub>2</sub>O<sub>4</sub> core-shell nanorattles are discussed below.

#### SiO<sub>2</sub>@MnCo<sub>2</sub>O<sub>4</sub> core-shell nanorattles

Phase analysis. Pure MnCo<sub>2</sub>O<sub>4</sub> NPs and SiO<sub>2</sub>@MnCo<sub>2</sub>O<sub>4</sub> core-shell NPs were obtained on calcination of MnCo-LDH and SiO<sub>2</sub>@MnCo-LDH samples at 500 °C, respectively. The XRD patterns of the MnCo<sub>2</sub>O<sub>4</sub> and SiO<sub>2</sub>@MnCo<sub>2</sub>O<sub>4</sub> samples are shown in Fig. 1. The XRD pattern of MnCo<sub>2</sub>O<sub>4</sub> matches with the pattern of cubic MnCo<sub>2</sub>O<sub>4</sub> (JCPDS file no. 23-1237). The peaks observed at  $2\theta = 18.1^{\circ}$ ,  $30.4^{\circ}$ ,  $35.9^{\circ}$ ,  $43.9^{\circ}$ ,  $53.5^{\circ}$ ,  $58.4^{\circ}$ , and  $64.5^{\circ}$  are ascribed to (111), (220), (311), (400), (422), (511), and (440) reflections of cubic MnCo<sub>2</sub>O<sub>4</sub>. The XRD patterns of the SiO<sub>2</sub>@MnCo<sub>2</sub>O<sub>4</sub>-0.25 and SiO<sub>2</sub>@MnCo<sub>2</sub>O<sub>4</sub>-0.5 samples show peaks at  $2\theta = 35.9^{\circ}$  and  $64.5^{\circ}$  attributed to the (311) and (440) planes of MnCo<sub>2</sub>O<sub>4</sub>.

The XRD pattern of  $SiO_2@MnCo_2O_4$ -1 shows peaks at  $2\theta$  =  $18.1^{\circ}$ ,  $30.2^{\circ}$ ,  $35.9^{\circ}$ ,  $43.7^{\circ}$ ,  $58.3^{\circ}$ , and  $64.3^{\circ}$  due to (111), (220), (311), (400), (511), and (440) reflections of MnCo<sub>2</sub>O<sub>4</sub>. The estimated crystallite size (using the Scherrer formula) of  $MnCo_2O_4$  are 9.3 nm, 6.4 nm, 3.5 nm, and 7.5 nm for  $MnCo_2O_4$ , SiO<sub>2</sub>@MnCo<sub>2</sub>O<sub>4</sub>-0.25, SiO<sub>2</sub>@MnCo<sub>2</sub>O<sub>4</sub>-0.5, and SiO<sub>2</sub>@Mn-Co<sub>2</sub>O<sub>4</sub>-1, respectively. The SiO<sub>2</sub>@MnCo<sub>2</sub>O<sub>4</sub> samples possess smaller crystallites of MnCo2O4 compared to pristine MnCo2O4 NPs.

#### FT-IR analysis

Fig. S5 (ESI†) displays the FT-IR spectra of MnCo<sub>2</sub>O<sub>4</sub> and SiO<sub>2</sub>@MnCo<sub>2</sub>O<sub>4</sub> samples (SiO<sub>2</sub>@MnCo<sub>2</sub>O<sub>4</sub>-0.25, SiO<sub>2</sub>@Mn-Co<sub>2</sub>O<sub>4</sub>-0.5, and SiO<sub>2</sub>@MnCo<sub>2</sub>O<sub>4</sub>-1). The IR spectra of all the samples exhibit bands at about 3438 cm<sup>-1</sup>, and 1637 cm<sup>-1</sup> assigned to stretching and bending vibrational modes of physisorbed H<sub>2</sub>O molecules. The IR spectrum of MnCo<sub>2</sub>O<sub>4</sub> shows IR bands around 659 cm<sup>-1</sup> and 568 cm<sup>-1</sup> attributed to stretching vibration of Co-O and Mn-O bonds, respectively. 14 The IR spectra of all the SiO<sub>2</sub>@MnCo<sub>2</sub>O<sub>4</sub> samples display characteristic bands of SiO<sub>2</sub> at 1105 cm<sup>-1</sup> and 486 cm<sup>-1</sup> due to v-(Si-O-Si) and δ-(Si-O-Si), respectively.<sup>5</sup> In the IR spectra of the SiO<sub>2</sub>@Mn-Co<sub>2</sub>O<sub>4</sub> samples, the bands observed at about 660 cm<sup>-1</sup> and 565 cm<sup>-1</sup> are assigned to the stretching vibrations of Co-O and Mn-O bonds, respectively. 14

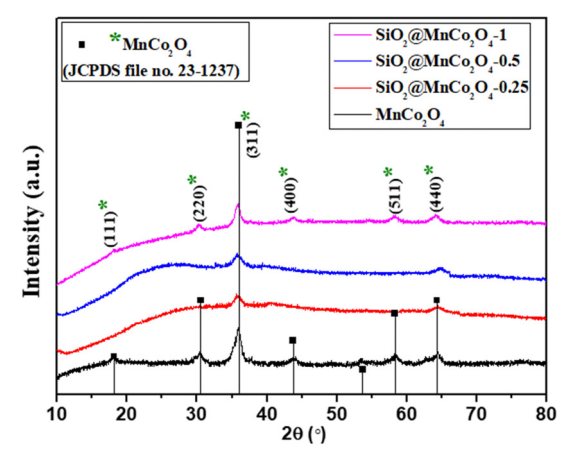


Fig. 1 XRD patterns of MnCo<sub>2</sub>O<sub>4</sub> and SiO<sub>2</sub>@MnCo<sub>2</sub>O<sub>4</sub> samples obtained by calcination of LDH precursors (Table 1) at 500 °C.

#### Morphological studies and elemental analysis

Fig. 2(a-d) displays FESEM images of pure MnCo<sub>2</sub>O<sub>4</sub> and SiO<sub>2</sub>@MnCo<sub>2</sub>O<sub>4</sub> samples (SiO<sub>2</sub>@MnCo<sub>2</sub>O<sub>4</sub>-0.25, SiO<sub>2</sub>@Mn-Co<sub>2</sub>O<sub>4</sub>-0.5, and SiO<sub>2</sub>@MnCo<sub>2</sub>O<sub>4</sub>-1). The FESEM image of pure MnCo<sub>2</sub>O<sub>4</sub>, (Fig. 2(a)) shows nanosheets (flake-like structures). The FESEM images of the SiO<sub>2</sub>@MnCo<sub>2</sub>O<sub>4</sub> samples (Fig. 2(b-d)) show that the SiO<sub>2</sub> spheres are uniformly covered with MnCo<sub>2</sub>O<sub>4</sub> nanoparticles. Table S4 (ESI†) summarizes the EDX analysis results for all SiO2@MnCo2O4 samples (after calcination at 500 °C). The results indicate that Si, Mn, Co, and O are present uniformly in all the SiO2@MnCo2O4 core-shell NPs. The weight % of Mn and Co in the SiO<sub>2</sub>@MnCo<sub>2</sub>O<sub>4</sub> samples varies according to the [Mn2+]:[Co2+] ratio used during the synthesis of their precursors (SiO<sub>2</sub>@MnCo-LDH).

Fig. 3(a-e) shows the TEM images of SiO<sub>2</sub>, pristine MnCo<sub>2</sub>O<sub>4</sub>, and SiO2@MnCo2O4 samples (SiO2@MnCo2O4-0.25, SiO2@Mn-Co<sub>2</sub>O<sub>4</sub>-0.5, and SiO<sub>2</sub>@MnCo<sub>2</sub>O<sub>4</sub>-1). A summary of the TEM results is given in Table 2. The TEM image of SiO<sub>2</sub> (Fig. 3(a)) shows spherical particles with mean diameter of 175  $\pm$  14 nm. Fig. 3(b) displays the TEM image of pristine MnCo<sub>2</sub>O<sub>4</sub>, showing its flakelike morphology (nanosheet). The mean thickness of MnCo<sub>2</sub>O<sub>4</sub> nanosheets is 9.3  $\pm$  3.6 nm. The TEM images (Fig. 3(c-e)) of SiO<sub>2</sub>@MnCo<sub>2</sub>O<sub>4</sub> samples (SiO<sub>2</sub>@MnCo<sub>2</sub>O<sub>4</sub>-0.25, SiO<sub>2</sub>@MnCo<sub>2</sub>O<sub>4</sub>-0.5, and SiO<sub>2</sub>@MnCo<sub>2</sub>O<sub>4</sub>-1) show interstitial space (void) between the core (SiO<sub>2</sub>) and the shell (MnCo<sub>2</sub>O<sub>4</sub>). Such nanoparticles are known in the literature as core-shell nanorattles or nanoparticles with yolk-shell morphology. 37,38 The TEM images also reveal that the MnCo<sub>2</sub>O<sub>4</sub> shell has a porous flower-like structure. From Table 2, it is observed that the mean size of the SiO<sub>2</sub> core in the  $SiO_2$ (a)MnCo<sub>2</sub>O<sub>4</sub> core-shell nanorattles varies from 171  $\pm$  13 nm to  $190 \pm 15$  nm. The mean thickness of the MnCo<sub>2</sub>O<sub>4</sub> shell lies in the range of 38  $\pm$  8 nm to 60  $\pm$  12 nm. The average void distance between the SiO<sub>2</sub> core and MnCo<sub>2</sub>O<sub>4</sub> shell varies from 16  $\pm$  3 nm to 30  $\pm$  6 nm. The mean thickness of the nanosheets of MnCo<sub>2</sub>O<sub>4</sub> (shell) in the SiO<sub>2</sub>@MnCo<sub>2</sub>O<sub>4</sub> core-shell nanorattles varies from 2.6  $\pm$  0.9 nm to 3.3  $\pm$  0.4 nm. The synthetic conditions play an

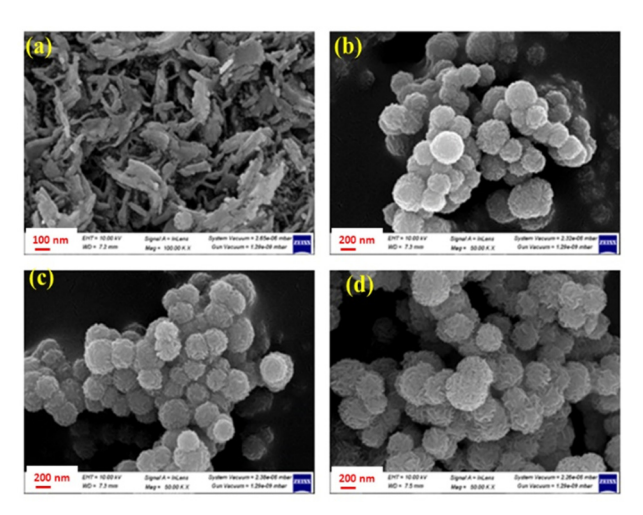


Fig. 2 FE-SEM images of (a) MnCo<sub>2</sub>O<sub>4</sub>, (b) SiO<sub>2</sub>@MnCo<sub>2</sub>O<sub>4</sub>-0.25, (c)  $SiO_2@MnCo_2O_4-0.5$ , and (d)  $SiO_2@MnCo_2O_4-1$  core-shell samples calcined at 500 °C.

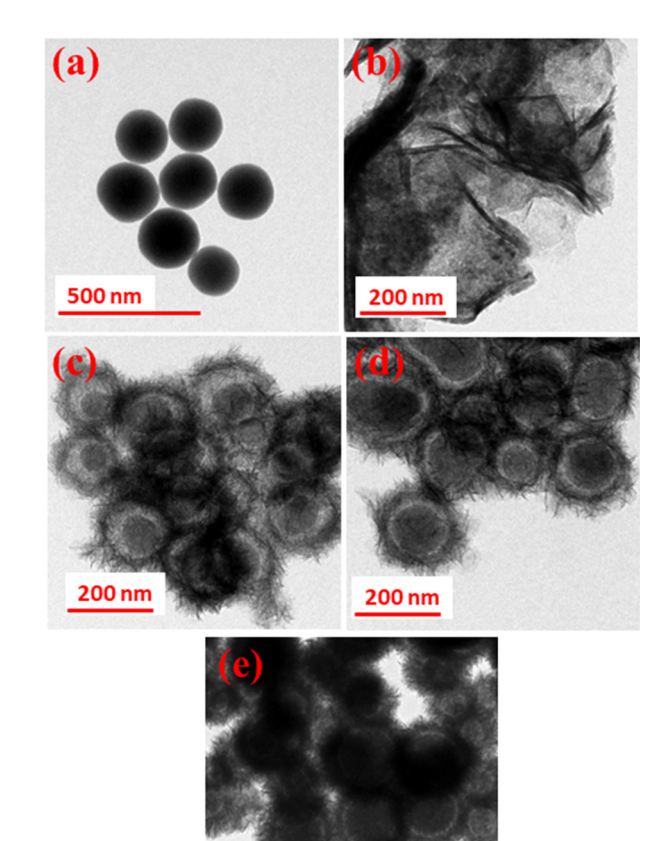


Fig. 3 TEM images of (a) SiO<sub>2</sub>, (b) MnCo<sub>2</sub>O<sub>4</sub>, (c) SiO<sub>2</sub>@MnCo<sub>2</sub>O<sub>4</sub>-0.25, (d)  $SiO_2@MnCo_2O_4-0.5$  and (e)  $SiO_2@MnCo_2O_4-1$  core-shell samples calcined at 500 °C

Table 2 Summary of TEM results of SiO2@MnCo2O4 core-shell nanorattles

Sample code	Core size (nm)			Flake thickness in the shell (nm)
SiO <sub>2</sub> @MnCo <sub>2</sub> O <sub>4</sub> -0.25 SiO <sub>2</sub> @MnCo <sub>2</sub> O <sub>4</sub> -0.5 SiO <sub>2</sub> @MnCo <sub>2</sub> O <sub>4</sub> -1		$41\pm10$	$16\pm3$	$2.6 \pm 0.9$ $3.2 \pm 0.6$ $3.3 \pm 0.4$

important role in the nanorattle formation. As the concentration (molar ratio) of metal salts used during the synthesis of SiO<sub>2</sub>@MnCo-LDH precursors (i.e. Mn(NO<sub>3</sub>)<sub>2</sub>·4H<sub>2</sub>O and Co(NO<sub>3</sub>)<sub>2</sub>· 6H<sub>2</sub>O) increases from 0.25:0.5 to 1:2, more MnCo<sub>2</sub>O<sub>4</sub> NPs are formed on the surface of the SiO<sub>2</sub> spheres, which leads to a thick coating of MnCo<sub>2</sub>O<sub>4</sub> NPs on the surface of the SiO<sub>2</sub> spheres. When lower concentration of metal salts is used, a thin coating of MnCo<sub>2</sub>O<sub>4</sub> NPs occurs and thus in the SiO<sub>2</sub>@MnCo<sub>2</sub>O<sub>4</sub>-0.25 sample, the thin coating of MnCo<sub>2</sub>O<sub>4</sub> leads to a good TEM image. EDS mapping and elemental line profiles of SiO<sub>2</sub>@MnCo<sub>2</sub>O<sub>4</sub> from TEM measurements were done and the results are shown in Fig. S6 and S7 (ESI†). The EDS elemental mapping images and elemental line profile of the SiO<sub>2</sub>@MnCo<sub>2</sub>O<sub>4</sub> core-shell nanorattles indicate

uniform distribution of elements (Si, Mn, Co and O) in the SiO<sub>2</sub>@MnCo<sub>2</sub>O<sub>4</sub> core-shell nanorattles. The line scan EDS images show that the Mn and Co content is more towards the edge of the spherical particles and the Si content is more in the center of the particles. This suggests coating of MnCo<sub>2</sub>O<sub>4</sub> on the SiO<sub>2</sub> spheres.

The SAED patterns of pure MnCo<sub>2</sub>O<sub>4</sub> NPs and SiO<sub>2</sub>(a) MnCo<sub>2</sub>O<sub>4</sub> samples (SiO<sub>2</sub>@MnCo<sub>2</sub>O<sub>4</sub>-0.25, SiO<sub>2</sub>@MnCo<sub>2</sub>O<sub>4</sub>-0.5, and SiO<sub>2</sub>@MnCo<sub>2</sub>O<sub>4</sub>-1) are displayed in Fig. S8(a-d) (ESI†). The SAED pattern of pure MnCo<sub>2</sub>O<sub>4</sub> (Fig. S8(a), ESI†) shows rings which indicate the polycrystalline nature of the MnCo<sub>2</sub>O<sub>4</sub> NPs. The observed rings are attributed to (220), (311), (400), (422), and (440) reflections of cubic MnCo<sub>2</sub>O<sub>4</sub>. The SAED patterns of SiO<sub>2</sub>@MnCo<sub>2</sub>O<sub>4</sub>-0.25, SiO<sub>2</sub>@MnCo<sub>2</sub>O<sub>4</sub>-0.5, and SiO<sub>2</sub>@Mn-Co<sub>2</sub>O<sub>4</sub>-1 core-shell nanorattles (Fig. S8(b-d), ESI†) also show rings, which suggests the polycrystalline nature of all the SiO<sub>2</sub>@MnCo<sub>2</sub>O<sub>4</sub> nanorattles. The observed rings correspond to the (311) and (422) planes of cubic MnCo<sub>2</sub>O<sub>4</sub>.

## BET surface area analysis

BET surface area measurements were carried out to determine the surface area, pore size, and pore volume of the SiO<sub>2</sub>@Mn-Co<sub>2</sub>O<sub>4</sub> core-shell nanorattles. SiO<sub>2</sub> and MnCo<sub>2</sub>O<sub>4</sub> nanoparticles exhibit a surface area of 88 m<sup>2</sup> g<sup>-1</sup> and 79 m<sup>2</sup> g<sup>-1</sup>, respectively. The core-shell nanorattles (SiO<sub>2</sub>@MnCo<sub>2</sub>O<sub>4</sub>-0.25, SiO<sub>2</sub>@Mn-Co<sub>2</sub>O<sub>4</sub>-0.5, and SiO<sub>2</sub>(aMnCo<sub>2</sub>O<sub>4</sub>-1) exhibit surface area of  $278 \text{ m}^2 \text{ g}^{-1}$ ,  $302 \text{ m}^2 \text{ g}^{-1}$ , and  $356 \text{ m}^2 \text{ g}^{-1}$ , respectively. The higher surface area of the SiO<sub>2</sub>@MnCo<sub>2</sub>O<sub>4</sub> nanorattles is attributed to the void space between the core (SiO<sub>2</sub>) and the shell (MnCo<sub>2</sub>O<sub>4</sub>). Adsorption-desorption isotherms were recorded for pure MnCo<sub>2</sub>O<sub>4</sub> nanoparticles and SiO<sub>2</sub>@MnCo<sub>2</sub>O<sub>4</sub>-1. As shown in Fig. S9(a) (ESI†), the adsorption-desorption isotherm of the MnCo<sub>2</sub>O<sub>4</sub> nanoparticles shows the characteristics of a porous material with open wedge pores. The adsorptiondesorption isotherm of SiO<sub>2</sub>@MnCo<sub>2</sub>O<sub>4</sub>-1 (Fig. S9(b), ESI†) matches with a type IV isotherm. 39 The MnCo<sub>2</sub>O<sub>4</sub> nanoparticles exhibit an average pore size and pore volume of 6.2 nm and 0.12 cm<sup>3</sup> g<sup>-1</sup>, respectively. The SiO<sub>2</sub>@MnCo<sub>2</sub>O<sub>4</sub>-1 exhibits an average pore size and pore volume of 5.0 nm and 0.44 cm<sup>3</sup> g<sup>-1</sup>, respectively.

# Mechanism of formation of SiO<sub>2</sub>@MnCo<sub>2</sub>O<sub>4</sub> core-shell

Fig. S10 (ESI†) shows the proposed mechanism of formation of SiO<sub>2</sub>@MnCo<sub>2</sub>O<sub>4</sub> core-shell nanorattles. In the first step, Mn<sup>2+</sup> and Co<sup>2+</sup> ions from the aqueous solution attach to the OH groups present on the surface of the SiO2 spheres via electrostatic interaction. At 85 °C, hydrolysis of urea leads to the production of NH4+ and OH- ions. The OH- ions react with Mn<sup>2+</sup> and Co<sup>2+</sup> ions present on the surface of SiO<sub>2</sub> forming MnCo-LDH via nucleation and coalescence processes. Finally, flower-like structures consisting of MnCo-LDH nanosheets are formed on the surface of the SiO2 spheres via Ostwald ripening. 40,41 The flower-like SiO<sub>2</sub> (a)MnCo-LDH precursors are converted into SiO<sub>2</sub>@MnCo<sub>2</sub>O<sub>4</sub> core-shell nanorattles via calcination at 500 °C with retention of the morphology.

Time-dependent TEM studies were carried out to understand better the formation of SiO<sub>2</sub>@MnCo-LDH nanorattles. The TEM images of SiO<sub>2</sub>@MnCo-LDH-0.25 recorded after different reaction times (1 h, 2 h, 3 h, 4 h, and 6 h) are shown in Fig. S11 (ESI†). After a reaction time of 1 h, MnCo-LDH crystallites are loosely attached on the outer surface of the SiO<sub>2</sub> spheres. These MnCo-LDH crystallites act as seed for the nucleation and recrystallization. As the reaction progresses (2 h, 4 h), Ostwald ripening (inside-out) dominates and smaller crystallites of MnCo-LDH present in the interior region dissolve, which initiates the hollowing process. Finally, after 6 h, a close-packed MnCo-LDH shell is formed on the surface of the SiO<sub>2</sub> spheres with a void space between the core and shell. SiO<sub>2</sub>@MnCo<sub>2</sub>O<sub>4</sub> core-shell nanorattles are obtained on calcination of SiO<sub>2</sub>@MnCo-LDH at 500 °C with the retention of the morphological features of the LDH precursor.

## Optical properties of SiO2@MnCo2O4 core-shell nanorattles

The optical properties of MnCo<sub>2</sub>O<sub>4</sub> nanoparticles and SiO<sub>2</sub>@MnCo<sub>2</sub>O<sub>4</sub> core-shell nanorattles were studied using UV-Vis diffuse reflectance spectroscopy (DRS). The UV-Vis DRS spectra of the MnCo2O4 nanoparticles and SiO2@MnCo2O4 core-shell nanorattles are shown in Fig. S12 (ESI†). The DRS spectra of the MnCo2O4 NPs and SiO2@MnCo2O4 nanorattles show broad bands at 250 nm and 470 nm, attributed to  $O^{2-} \rightarrow$  $Mn^{2+}$  and  $O^{2-} \rightarrow Co^{3+}$  charge-transfer transitions of MnCo<sub>2</sub>O<sub>4</sub>, respectively. 43,44 The DRS spectra of all the samples exhibit a broad band at about 738 nm due to d-d transitions of Mn<sup>2+</sup> and Co3+ of MnCo2O4 NPs.42,43

## XPS analysis

The oxidation states of Si, Mn, Co, and O in SiO<sub>2</sub>, MnCo<sub>2</sub>O<sub>4</sub> NPs and SiO<sub>2</sub>@MnCo<sub>2</sub>O<sub>4</sub>-1 nanorattles were determined using XPS analysis.

Fig. S13 (ESI†) displays the XPS spectrum of SiO<sub>2</sub>. The Si 2p spectrum of SiO2 shows a peak at 103.8 eV, indicating the existence of Si4+. The O 1s spectrum of SiO2 shows peaks at 532.7 eV and 533.8 eV, indicating the existence of lattice oxygen and surface hydroxyl oxygen in SiO<sub>2</sub>, respectively. 44 Fig. 4(a and b) shows the XPS spectra of pure MnCo2O4 NPs and SiO2@Mn- $Co_2O_4$ -1. The Mn 2p spectrum of pure Mn $Co_2O_4$  NPs (Fig. 4(a)) shows peaks due to Mn  $2p_{3/2}$  (642.1 eV (Mn<sup>2+</sup>) and 643.5 eV  $(Mn^{3+})$  and Mn  $2p_{1/2}$  (654.0 eV). The Co 2p spectrum of MnCo<sub>2</sub>O<sub>4</sub> NPs (Fig. 4(a)) shows peaks due to Co 2p<sub>3/2</sub> (780.1 eV ( $Co^{2+}$ ) and 782.1 eV ( $Co^{3+}$ ) and Co  $2p_{1/2}$  (795.2 eV  $(Co^{2+})$  and 797.3 eV  $(Co^{3+})$ ). The peaks observed at 788.0 eV and 803.8 eV correspond to satellite peaks. The O 1s spectrum of pure MnCo2O4 NPs shows peaks at 530.1 eV and 531.9 eV, assigned to lattice oxygen of MnCo2O4 and surface hydroxyl oxygen, respectively. 45,46 The Si 2p XPS spectrum of SiO<sub>2</sub>(a) MnCo<sub>2</sub>O<sub>4</sub>-1 (Fig. 4(b)) shows a peak at 102.7 eV, suggesting the presence of Si<sup>4+</sup>. The Mn 2p spectrum of SiO<sub>2</sub>@MnCo<sub>2</sub>O<sub>4</sub>-1 (Fig. 4b) exhibits peaks due to Mn  $2p_{3/2}$  (642.2 eV (Mn<sup>2+</sup>) and 644 eV (Mn<sup>3+</sup>)) and Mn 2p<sub>1/2</sub> (654.2 eV (Mn<sup>3+</sup>)). The Co 2p spectrum of SiO<sub>2</sub>@MnCo<sub>2</sub>O<sub>4</sub>-1 (Fig. 4b) shows peaks due to Co  $2p_{3/2}$  (781.1 eV (Co<sup>2+</sup>) and 782.7 eV (Co<sup>3+</sup>)) and Co  $2p_{1/2}$ 

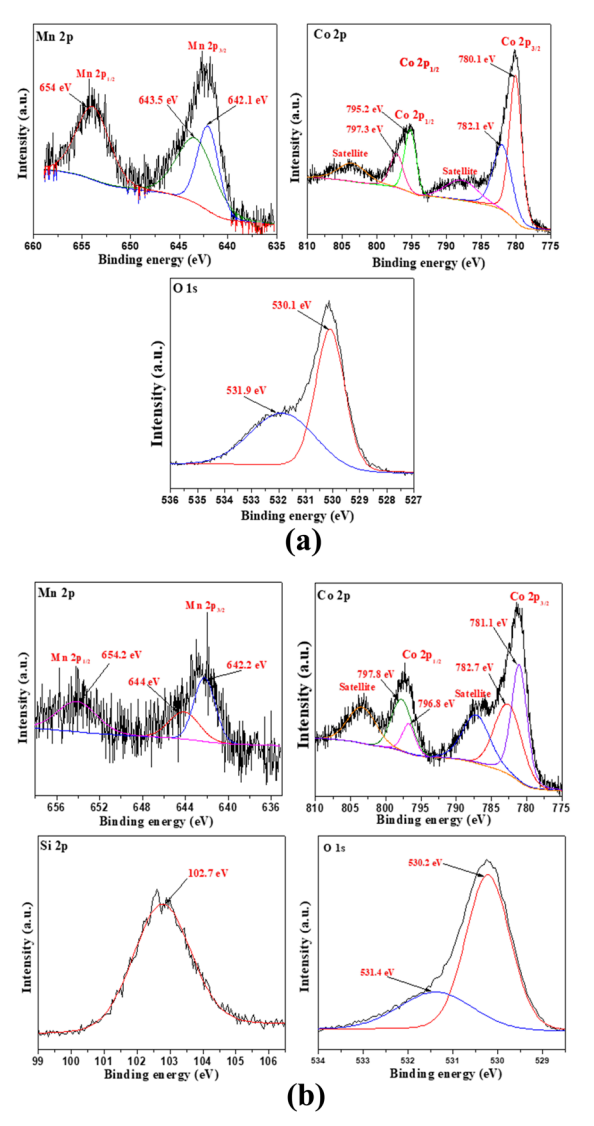


Fig. 4 XPS spectra of (a) MnCo<sub>2</sub>O<sub>4</sub> NPs and (b) SiO<sub>2</sub>@MnCo<sub>2</sub>O<sub>4</sub>-1 coreshell nanoparticles calcined at 500 °C.

(796.8 eV (Co<sup>2+</sup>) and 797.8 eV (Co<sup>3+</sup>)). Two satellite peaks are also observed at 787.5 eV and 803.5 eV. The O 1s spectrum of SiO<sub>2</sub>@MnCo<sub>2</sub>O<sub>4</sub>-1 (Fig. 4b) exhibits peaks at 530.2 eV and 531.4 eV due to lattice oxygen of MnCo<sub>2</sub>O<sub>4</sub> and surface hydroxyl oxygen, respectively.44-46

#### Magnetic properties

Magnetic hysteresis (M-H) plots of pure MnCo2O4 NPs and SiO<sub>2</sub>@MnCo<sub>2</sub>O<sub>4</sub> nanorattles were recorded at RT (300 K) and 5 K up to an applied field of 40 kOe. The M-H curves of pure MnCo<sub>2</sub>O<sub>4</sub> NPs and SiO<sub>2</sub>@MnCo<sub>2</sub>O<sub>4</sub> samples (SiO<sub>2</sub>@MnCo<sub>2</sub>O<sub>4</sub>-0.25, SiO<sub>2</sub>@MnCo<sub>2</sub>O<sub>4</sub>-0.5, and SiO<sub>2</sub>@MnCo<sub>2</sub>O<sub>4</sub>-1) are shown in Fig. 5. At 300 K, the absence of hysteresis and negligible coercivity indicate paramagnetic nature of the pure MnCo<sub>2</sub>O<sub>4</sub> NPs and all the SiO<sub>2</sub>@MnCo<sub>2</sub>O<sub>4</sub> samples. Table 3 gives the coercivity and magnetization values of pure MnCo2O4 NPs and SiO<sub>2</sub>@MnCo<sub>2</sub>O<sub>4</sub> samples at 5 K. At 5 K, the M-H hysteresis loop

of the MnCo2O4 nanoparticles exhibits coercivity of 5.0 kOe and magnetization of 6.8 emu g<sup>-1</sup> (@40 kOe), indicating hard ferromagnetic behavior. At 5 K, the negligible coercivity and finite magnetization of all the SiO<sub>2</sub>@MnCo<sub>2</sub>O<sub>4</sub> samples indicate superparamagnetic behavior. The coercivity values for SiO<sub>2</sub>@MnCo<sub>2</sub>O<sub>4</sub>-0.25, SiO<sub>2</sub>@MnCo<sub>2</sub>O<sub>4</sub>-0.5, and SiO<sub>2</sub>@MnCo<sub>2</sub>O<sub>4</sub>-1 at 5 K are 0.05 kOe, 0.02 kOe, and 0.09 kOe, respectively. For SiO<sub>2</sub>@MnCo<sub>2</sub>O<sub>4</sub>-0.25, SiO<sub>2</sub>@MnCo<sub>2</sub>O<sub>4</sub>-0.5, and SiO<sub>2</sub>@MnCo<sub>2</sub>O<sub>4</sub>-1, the magnetization values (@40 kOe) at 5 K are 46.5 emu g<sup>-1</sup>, 36.3 emu  $g^{-1}$ , and 25.5 emu  $g^{-1}$ , respectively.

At low temperature, the dominance of magneto-crystalline anisotropy leads to higher coercivity and magnetization of the MnCo<sub>2</sub>O<sub>4</sub> nanoparticles and SiO<sub>2</sub>@MnCo<sub>2</sub>O<sub>4</sub> samples.<sup>47</sup> The lower coercivity of SiO2@MnCo2O4 nanorattles compared to pure MnCo<sub>2</sub>O<sub>4</sub> nanoparticles is attributed to the diamagnetic SiO<sub>2</sub> phase in the nanorattles. 48 The higher magnetization of SiO<sub>2</sub>@MnCo<sub>2</sub>O<sub>4</sub> samples compared to pure MnCo<sub>2</sub>O<sub>4</sub> NPs is attributed to smaller crystallite size of MnCo2O4 NPs in the SiO<sub>2</sub>@MnCo<sub>2</sub>O<sub>4</sub> samples. In the MnCo<sub>2</sub>O<sub>4</sub> nanoparticles,  $SiO_2$ @MnCo<sub>2</sub>O<sub>4</sub>-0.25,  $SiO_2$ @MnCo<sub>2</sub>O<sub>4</sub>-0.5, and MnCo<sub>2</sub>O<sub>4</sub>-1, the crystallite size of MnCo<sub>2</sub>O<sub>4</sub> are 9.3 nm, 6.4 nm, 3.5 nm, and 7.5 nm, respectively. The ZFC and FC magnetization curves recorded under 2 kOe for pure MnCo2O4 NPs and SiO<sub>2</sub>@MnCo<sub>2</sub>O<sub>4</sub> nanorattles (SiO<sub>2</sub>@MnCo<sub>2</sub>O<sub>4</sub>-0.25, SiO<sub>2</sub>@MnCo<sub>2</sub>O<sub>4</sub>-0.5, and SiO<sub>2</sub>@MnCo<sub>2</sub>O<sub>4</sub>-1) are shown in Fig. 6. The ZFC and FC curves of pure MnCo<sub>2</sub>O<sub>4</sub> NPs display a bifurcation at about 100 K and a hump at 25 K, which are assigned as irreversible temperature  $(T_{irr})$  and blocking temperature (T<sub>B</sub>), respectively. All the SiO<sub>2</sub>@MnCo<sub>2</sub>O<sub>4</sub> core-shell nanorattles show overlapped ZFC and FC curves without any hump, indicating superparamagnetic nature of the samples despite the absence of a maximum in the ZFC curve. The absence of maxima in the ZFC curves of the SiO2@MnCo2O4 samples is due to the absence of ferrimagnetic ordering in these samples. 49-52

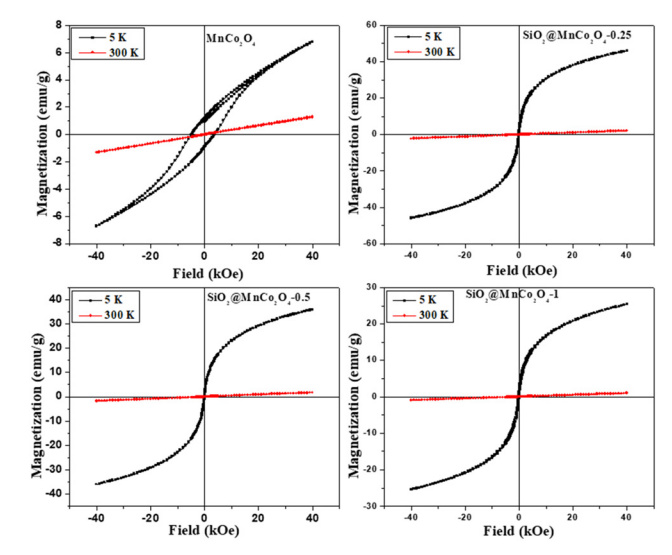


Fig. 5 M-H curves for MnCo<sub>2</sub>O<sub>4</sub> NPs and SiO<sub>2</sub>@MnCo<sub>2</sub>O<sub>4</sub> core-shell nanorattles at 300 K and 5 K.

Table 3 Summary of magnetic parameters of MnCo<sub>2</sub>O<sub>4</sub> NPs and SiO<sub>2</sub>@MnCo<sub>2</sub>O<sub>4</sub> core-shell NPs at 5 K

Sample code	Coercivity (H <sub>c</sub> , kOe)	Magnetization (emu g <sup>-1</sup> )	Crystallite size (nm)
MnCo <sub>2</sub> O <sub>4</sub>	5.00	6.8	9.3
SiO <sub>2</sub> @MnCo <sub>2</sub> O <sub>4</sub> -0.25	0.05	46.5	6.4
SiO <sub>2</sub> @MnCo <sub>2</sub> O <sub>4</sub> -0.5	0.02	36.3	3.5
SiO <sub>2</sub> @MnCo <sub>2</sub> O <sub>4</sub> -1	0.09	25.5	7.5

## Peroxidase-like activity of SiO2@MnCo2O4 nanorattles

The current study demonstrates the peroxidase-like activity of pure MnCo<sub>2</sub>O<sub>4</sub> nanoparticles and SiO<sub>2</sub>@MnCo<sub>2</sub>O<sub>4</sub> core-shell nanorattles (SiO<sub>2</sub>@MnCo<sub>2</sub>O<sub>4</sub>-0.25, SiO<sub>2</sub>@MnCo<sub>2</sub>O<sub>4</sub>-0.5, and SiO<sub>2</sub>@Mn-Co<sub>2</sub>O<sub>4</sub>-1). The SiO<sub>2</sub>@MnCo<sub>2</sub>O<sub>4</sub> core-shell nanorattles were tested as catalyst for peroxidase-like activity using TMB and H2O2 as substrate and oxidizing agent, respectively. The oxidation of TMB using SiO2@MnCo2O4 core-shell nanorattles in the presence of H<sub>2</sub>O<sub>2</sub> leads to formation of TMB<sup>•+</sup> (blue-colored charge transfer complex). The UV-Vis spectrum of TMB<sup>•+</sup> consists of a characteristic absorption maximum at 652 nm.<sup>28</sup> An intense blue-colored solution is obtained using SiO<sub>2</sub>@MnCo<sub>2</sub>O<sub>4</sub> as the catalyst compared to pure MnCo<sub>2</sub>O<sub>4</sub> NPs, which suggests the role of SiO<sub>2</sub>(a) MnCo<sub>2</sub>O<sub>4</sub> as the catalyst in peroxidase-like activity.

The UV-Vis spectral results (abs. vs. time plots) and % relative efficiency of peroxidase-like activity for pure MnCo2O4 NPs and SiO<sub>2</sub>@MnCo<sub>2</sub>O<sub>4</sub> core-shell NPs are shown in Fig. 7 and Fig. S14 (ESI†), respectively. As shown in Fig. 7, compared to pure MnCo2O4 nanoparticles, SiO2@MnCo2O4 nanorattles show better peroxidase-like activity. SiO<sub>2</sub>@MnCo<sub>2</sub>O<sub>4</sub>-1 exhibits the best peroxidase-like activity among the SiO2@MnCo2O4 samples.

## Influence of physicochemical conditions on the peroxidase-like activity

In the current study, various experimental parameters were varied to achieve optimal conditions for the peroxidase-like

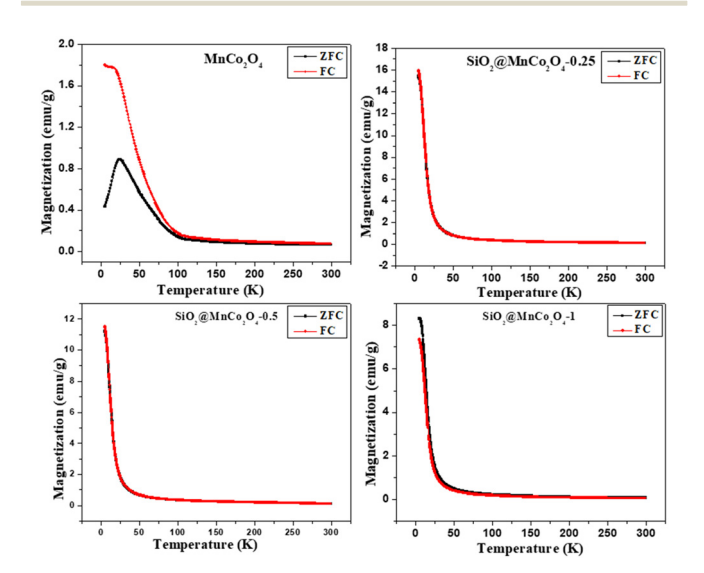


Fig. 6 ZFC and FC curves for MnCo<sub>2</sub>O<sub>4</sub> NPs and SiO<sub>2</sub>@MnCo<sub>2</sub>O<sub>4</sub> coreshell nanorattles

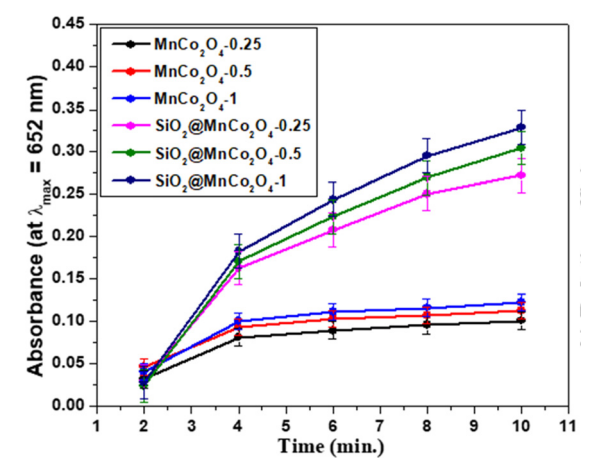


Fig. 7 Peroxidase-like activity of  $MnCo_2O_4$  NPs and  $SiO_2@MnCo_2O_4$ core-shell nanorattles as indicated by time dependent absorbance.

activity of the SiO<sub>2</sub>@MnCo<sub>2</sub>O<sub>4</sub> core-shell nanorattles. Studies were carried out to investigate the effect of varying pH (2-12) and amount of catalyst (5 µL - 60 µL of dispersion) on the peroxidase-like activity of the SiO2@MnCo2O4 core-shell nanorattles. The influence of varying pH (2-12) on the peroxidase-like activity (Fig. S15(a), ESI†) reveals the maximum peroxidase-like activity of  $SiO_2@MnCo_2O_4$  core-shell nanorattles at pH = 5. At low pH (<5), protonation of amino groups of TMB occurs. The protonation of amino groups leads to the retardation of electron transfer from the substrate (TMB) to the catalyst surface (SiO<sub>2</sub>@MnCo<sub>2</sub>O<sub>4</sub>-1). Hence, in a strongly acidic medium, the peroxidase-like activity of SiO<sub>2</sub>@MnCo<sub>2</sub>O<sub>4</sub>-1 decreases. When pH > 5, production of  $O_2$  and  $H_2O$  occurs via the break-down of H<sub>2</sub>O<sub>2</sub> in the presence of more hydroxyl ions, which leads to suppression of the peroxidase-like activity of SiO2@MnCo2O4-1.53,54 A linear variation of the peroxidase-like activity of SiO<sub>2</sub>@MnCo<sub>2</sub>O<sub>4</sub>-1 with an increment in catalyst dose from 5 μL to 60 μL of dispersion (1 mg catalyst dispersed by sonication in 1 mL H2O) is observed (Fig. S15(b), ESI†). A leaching experiment was carried out to understand further the peroxidase-like activity of SiO2@MnCo2O4-1. In a typical experiment, SiO<sub>2</sub>@MnCo<sub>2</sub>O<sub>4</sub>-1 (30 µL dispersion) was incubated in 3 mL buffer (pH = 5) for about 30 minutes. The supernatant solution obtained by centrifugation was further examined for peroxidase-like activity by adding TMB and H<sub>2</sub>O<sub>2</sub> solutions. The UV-Vis spectrum of the leached solution was recorded in kinetic mode up to 10 minutes (Fig. S16, ESI†). The negligible absorbance shown by the leached solution confirms the role of MnCo2O4 NPs in the peroxidase-like activity and the activity is not due to leached ions.

## Kinetic studies

Steady state-kinetic studies on the peroxidase-like activity of SiO<sub>2</sub>@MnCo<sub>2</sub>O<sub>4</sub>-1 nanorattles were performed using different substrates (i.e., TMB and  $H_2O_2$ ). The kinetic results at different TMB concentrations by fixing H<sub>2</sub>O<sub>2</sub> concentration and vice versa are shown in Fig. S17(a and b) (ESI†). The kinetic parameters  $(K_{\rm m}$  and  $V_{\rm max})$  were determined from the slope and

intercept values of Lineweaver-Burk reciprocal plots (Fig. S18(a and b), ESI†). The K<sub>m</sub> and V<sub>max</sub> values for SiO<sub>2</sub>@MnCo<sub>2</sub>O<sub>4</sub>-1 core-shell nanorattles are summarized in Table 4. Table 4 also gives the kinetic parameters for different metal oxide nanoparticles and core-shell NPs reported in the literature. 5,54-60 The Michaelis-Menten constant  $(K_m)$  is inversely proportional to the catalyst's affinity towards a substrate; a smaller  $K_{\rm m}$  value indicates higher affinity of a catalyst towards the substrate.<sup>54</sup> The K<sub>m</sub> and V<sub>max</sub> values for SiO<sub>2</sub>@MnCo<sub>2</sub>O<sub>4</sub>-1 core-shell nanorattles towards TMB are 0.032 mM and 1.596  $\times$  10<sup>-8</sup> Ms<sup>-1</sup>, respectively. The K<sub>m</sub> and V<sub>max</sub> values for SiO<sub>2</sub>@MnCo<sub>2</sub>O<sub>4</sub>-1 core-shell nanorattles towards H2O2 are 2.7 mM and  $0.532 \times 10^{-8} \text{ Ms}^{-1}$ , respectively. The reported  $K_{\rm m}$  and  $V_{\rm max}$ values for MnCo<sub>2</sub>O<sub>4</sub> nanoparticles towards TMB are 0.063 mM and  $2.17 \times 10^{-5} \text{ Ms}^{-1}$ , respectively.<sup>51</sup> For the natural peroxidase enzyme (HRP), the reported  $K_{\rm m}$  and  $V_{\rm max}$  values towards TMB are 0.434 mM and  $10 \times 10^{-8} \, \text{Ms}^{-1}$  and towards  $H_2O_2$ , the values are 3.70 mM and  $8.71 \times 10^{-8} \text{ Ms}^{-1}$ , respectively.<sup>55</sup> The observed K<sub>m</sub> value for SiO<sub>2</sub>@MnCo<sub>2</sub>O<sub>4</sub>-1 nanorattles towards TMB, in the present study, is smaller than that of MnCo<sub>2</sub>O<sub>4</sub> nanoparticles and natural peroxidase enzyme (HRP). These results indicate high affinity of SiO2@MnCo2O4-1 core-shell nanorattles towards TMB with better peroxidase-like activity.

## Mechanism of peroxidase-like activity of SiO<sub>2</sub>@MnCo<sub>2</sub>O<sub>4</sub> nanorattles

Fig. 8 shows the mechanism for the peroxidase-like activity of SiO<sub>2</sub>@MnCo<sub>2</sub>O<sub>4</sub> nanorattles. In the first step, adsorption of tetramethylbenzidine (TMB) molecules occurs on the surface of SiO<sub>2</sub>@MnCo<sub>2</sub>O<sub>4</sub> nanorattles. This promotes nitrogen electron pair donation from the NH2 groups of TMB towards the surface of SiO<sub>2</sub>@MnCo<sub>2</sub>O<sub>4</sub>, resulting in high electron density over SiO<sub>2</sub>@MnCo<sub>2</sub>O<sub>4</sub>. 31,54,61 The SiO<sub>2</sub>@MnCo<sub>2</sub>O<sub>4</sub> core-shell nanorattles reduce H2O2 into OH and OH species. The OH and OH• species facilitate the oxidation of TMB into TMB• (a blue-colored CT complex). The rattle-like hierarchical structure of MnCo<sub>2</sub>O<sub>4</sub> NPs present on the surface of SiO<sub>2</sub> spheres eases

**Table 4** Comparison of steady-state kinetic parameters ( $K_{\rm m}$  and  $V_{\rm max}$ ) for SiO2@MnCo2O4 core-shell nanorattles with those reported in the literature

Catalyst	Substrate	$K_{\rm m}$ (mM)	$V_{\rm max} \left({ m Ms}^{-1} ight)$	Reference
SiO <sub>2</sub> @Co <sub>3</sub> O <sub>4</sub> CSNPs	TMB	0.087	$0.012 \times 10^{-8}$	5
SiO <sub>2</sub> @Co <sub>3</sub> O <sub>4</sub> CSNPs	$H_2O_2$	25.2	$0.015 \times 10^{-8}$	5
MnCo <sub>2</sub> O <sub>4</sub> nanoparticles	TMB	0.063	$2.17 \times 10^{-5}$	54
HRP	TMB	0.434	$10.0 \times 10^{-8}$	54
HRP	$H_2O_2$	3.70	$8.71 \times 10^{-8}$	55
MnO <sub>2</sub> nanoparticles	TMB	0.04	$5.78 \times 10^{-6}$	56
Co <sub>3</sub> O <sub>4</sub> nanoparticles	TMB	0.037	$6.27 \times 10^{-8}$	57
Co <sub>3</sub> O <sub>4</sub> nanoparticles	$H_2O_2$	140.07	$12.1 \times 10^{-8}$	57
Co <sub>3</sub> O <sub>4</sub> @NiO CSNPs	TMB	0.036		58
Co <sub>3</sub> O <sub>4</sub> @NiO CSNPs	$H_2O_2$	8.17		58
Fe <sub>3</sub> O <sub>4</sub> @CoFe-LDH	TMB	0.395		59
Fe <sub>3</sub> O <sub>4</sub> @CoFe-LDH	$H_2O_2$	47.6		59
$TiO_2$ @ $CeO_x$	TMB	0.28	$6.5 \times 10^{-9}$	60
$TiO_2$ @ $CeO_x$	$H_2O_2$	6.29	$34 \times 10^{-9}$	60
SiO <sub>2</sub> @MnCo <sub>2</sub> O <sub>4</sub> -1	TMB	0.032	$1.596 \times 10^{-8}$	This work
$SiO_2@MnCo_2O_4$ -1	$H_2O_2$	2.7	$0.532 \times 10^{-8}$	This work

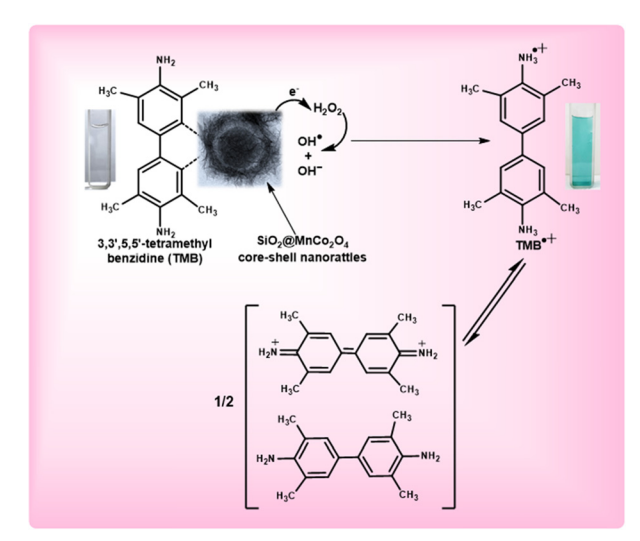


Fig. 8 Proposed mechanism of peroxidase-like activity of SiO<sub>2</sub>@Mn-Co<sub>2</sub>O<sub>4</sub> core-shell nanorattles using TMB as a substrate.

interaction between tetramethylbenzidine and the catalytic active centers (Mn<sup>2+</sup> and Co<sup>2+</sup>) leading to improved peroxidase-like activity of the SiO<sub>2</sub>@MnCo<sub>2</sub>O<sub>4</sub> nanorattles.

In the current study, high surface area and rattle-like morphology of SiO<sub>2</sub>@MnCo<sub>2</sub>O<sub>4</sub> lead to enhanced peroxidase-like activity. The higher peroxidase-like activity of SiO2@MnCo2O4-1 compared to the other samples is attributed to its high surface area (356 m<sup>2</sup> g<sup>-1</sup>). The SiO<sub>2</sub>@MnCo<sub>2</sub>O<sub>4</sub> core-shell nanorattles, synthesized in the current study, exhibit high surface area due to their rattle-type porous morphology. The high surface area of the SiO<sub>2</sub>@MnCo<sub>2</sub>O<sub>4</sub> core-shell nanorattles is helpful for enhanced peroxidase-like activity. The rattle-type porous nature of hierarchical MnCo<sub>2</sub>O<sub>4</sub> NPs on the surface of SiO<sub>2</sub> spheres provides less steric hindrance for the TMB molecules to interact with the catalytic centres (Mn<sup>2+</sup> and Co<sup>2+</sup>).<sup>62,63</sup> This promotes electron transfer from the SiO2@MnCo2O4 core-shell nanorattles towards H2O2 resulting in faster chemical reduction of  $H_2O_2$ .

Fig. S19 (ESI†) shows the fluorescence spectra for the detection of OH\*. radicals produced during the peroxidase-like activity. Terephthalic acid (probe molecule,  $\lambda_{exc}$  = 315 nm) produces fluorescent 2-hydroxyterephthalic acid ( $\lambda_{em}$  = 425 nm) on reacting with hydroxyl radicals. It can be noted that the fluorescence intensity increases with time due to increasing production of hydroxyl radicals. The PL results suggest the role of hydroxyl radicals in the peroxidase-like activity of SiO<sub>2</sub>@MnCo<sub>2</sub>O<sub>4</sub> nanorattles.

## Detection of H<sub>2</sub>O<sub>2</sub> using SiO<sub>2</sub>@MnCo<sub>2</sub>O<sub>4</sub> nanorattles

SiO<sub>2</sub>@MnCo<sub>2</sub>O<sub>4</sub> core-shell nanorattles were used for the detection of H<sub>2</sub>O<sub>2</sub> using peroxidase-like activity. A calibration plot (Fig. S20, ESI†) was recorded for SiO<sub>2</sub>@MnCo<sub>2</sub>O<sub>4</sub>-1 with varying concentration of  $H_2O_2$  (linear range = 0.05 mM to 1 mM). The equation given below was used for determining the limit of detection (LOD) of  $H_2O_2$ .

Limit of detection =  $3 \times (Standard deviation due to blank/$ Slope)

The standard deviation was estimated by recording the absorption spectra of a blank solution (i.e.  $[H_2O_2] = 0$ ) three times. The slope was calculated from the absorbance ( $@\lambda_{max} =$ 652 nm) versus [H<sub>2</sub>O<sub>2</sub>] plot (Fig. S20(b), ESI†). The estimated LOD value for H<sub>2</sub>O<sub>2</sub> using SiO<sub>2</sub>@MnCo<sub>2</sub>O<sub>4</sub> core-shell nanorattles is 0.083 mM and it is comparable with that reported in the literature. 58,63

## Conclusions

The current work demonstrates a simple and cost-effective synthetic strategy to synthesize SiO2@MnCo2O4 core-shell nanorattles via calcination of SiO2@MnCo-LDH precursors at 500 °C. MnCo<sub>2</sub>O<sub>4</sub> NPs deposit on the surface of SiO<sub>2</sub> spheres creating a hollow space (void) between the core and shell. The [Mn<sup>2+</sup>:Co<sup>2+</sup>] ratio affects thickness of the MnCo<sub>2</sub>O<sub>4</sub> shell and void distance between the core (SiO<sub>2</sub>) and the shell (MnCo<sub>2</sub>O<sub>4</sub>). XRD results confirm the formation of MnCo2O4 NPs in the SiO<sub>2</sub>@MnCo<sub>2</sub>O<sub>4</sub> samples. FESEM and TEM analyses show nanorattle-like morphology of all the SiO<sub>2</sub>@MnCo<sub>2</sub>O<sub>4</sub> samples. The mean shell thickness and void distance between the SiO<sub>2</sub> core and MnCo<sub>2</sub>O<sub>4</sub> shell in the SiO<sub>2</sub>@MnCo<sub>2</sub>O<sub>4</sub> core-shell nanorattles vary from 38  $\pm$  8 nm to 60  $\pm$  12 nm and 16  $\pm$ 3 nm to 30  $\pm$  6 nm, respectively. BET measurements indicate higher surface area of SiO2@MnCo2O4 core-shell nanorattles (278 m $^2$  g $^{-1}$  to 356 m $^2$  g $^{-1}$ ) compared to the constituents. XPS analysis confirms the presence of Si<sup>4+</sup>, Mn<sup>2+</sup>, Co<sup>2+</sup>, Mn<sup>3+</sup>, Co<sup>3+</sup>, and O<sup>2-</sup> in the SiO<sub>2</sub>@MnCo<sub>2</sub>O<sub>4</sub> nanorattles. Magnetic measurements indicate paramagnetic and superparamagnetic behavior of SiO<sub>2</sub>@MnCo<sub>2</sub>O<sub>4</sub> nanorattles at 300 K and 5 K, respectively. The SiO<sub>2</sub>@MnCo<sub>2</sub>O<sub>4</sub> nanorattles exhibit better peroxidase-like activity than pure MnCo<sub>2</sub>O<sub>4</sub> NPs and horseradish peroxidase. The peroxidase-like activity of the core-shell nanorattles can be useful for several sensing applications, such as the detection of glucose, H2O2, ascorbic acid, hydroquinone, protein, and dopamine.

## Conflicts of interest

There are no conflicts of interest to declare.

# Acknowledgements

Pankaj Rana expresses his gratitude to the UGC and the Ministry of Education, Government of India for awarding him a fellowship (JRF/SRF). The authors express gratitude to Institute Instrumentation Centre (IIC), IIT Roorkee for providing the necessary instrumentation facilities. The authors are also thankful to the Department of Metallurgical and Materials Engineering, IIT Roorkee for providing the TEM facility.

## References

- 1 A. M. El-Toni, M. A. Habila, J. P. Labis, Z. A. Alothman, M. Alhoshan, A. A. Elzatahry and F. Zhang, Nanoscale, 2016, 8, 2510-2531.
- 2 M. Priebe and K. M. Fromm, Chem. Eur. J., 2015, 21, 3854-3874.
- 3 J. Liu, R. Harrison, J. Z. Zhou, T. T. Liu, C. Yu, G. Q. Lu, S. Z. Qiao and Z. P. Xu, J. Mater. Chem., 2011, 21, 10641-10644.
- 4 J. Lee, J. C. Park and H. Song, Adv. Mater., 2008, 20, 1523-1528.
- 5 S. Kandula and P. Jeevanandam, RSC Adv., 2015, 5, 5295-5306.
- 6 J. S. Chen, C. M. Li, W. W. Zhou, Q. Y. Yan, L. A. Archer and X. W. Lou, Nanoscale, 2009, 1, 280-285.
- 7 A. Rokicinska, M. Zurowska, P. Łatka and P. Kustrowski, Catalysts, 2021, 11, 1097.
- 8 Y. Hu, X. T. Zheng, J. S. Chen, M. Zhou, C. M. Li and X. W. Lou, J. Mater. Chem., 2011, 21, 8052-8056.
- 9 B. J. Jankiewicz, D. Jamiola, J. Choma and M. Jaroniec, Adv. Colloid Interface Sci., 2012, 170, 28-47.
- 10 N. Yan, Z. Zhao, Y. Li, F. Wang, H. Zhong and Q. Chen, Inorg. Chem., 2014, 53, 9073-9079.
- 11 Y. Yu, M. Zhou, W. Zhang, L. Huang, D. Miao, H. Zhu and G. Su, Mol. Pharmaceutics, 2019, 16, 1929-1938.
- 12 C. Liu, J. Li, J. Qi, J. Wang, R. Luo, J. Shen, X. Sun, W. Han and L. Wang, ACS Appl. Mater. Interfaces, 2014, 6, 13167-13173.
- 13 T. Zhang, Z. Li, L. Wang, P. Sun, Z. Zhang and S. Wang, ChemSusChem, 2018, 11, 2730-2736.
- 14 T. Pettong, P. Iamprasertkun, A. Krittayavathananon, P. Sukha, Sirisinudomkit, A. Seubsai, M. Chareonpanich, P. Kongkachuichay, J. Limtrakul and M. Sawangphruk, ACS Appl. Mater. Interfaces, 2016, 8, 34045-34053.
- 15 B. Wang, S. Wang, Y. Tang, C. W. Tsang, J. Dai, M. K. H. Leung and X. Y. Lu, Appl. Energy, 2019, 252, 113452.
- 16 W. Yang, J. Hao, Z. Zhang, B. Lu, B. Zhang and J. Tang, Catal. Commun., 2014, 46, 174-178.
- 17 S. Tarighi and N. M. Juibari, ChemistrySelect, 2019, 4, 6506-6515.
- 18 Y. Liang, H. Wang, J. Zhou, Y. Li, J. Wang, T. Regier and H. Dai, J. Am. Chem. Soc., 2012, 134, 3517-3523.
- 19 X. Wang, L. Xu, K. Song, R. Yang, L. Jia, X. Guo, X. Jing and J. Wang, Colloids Surf., A, 2019, 570, 73-80.
- 20 Y. Zhao, L. Hu, S. Zhao and L. Wu, Adv. Funct. Mater., 2016, 26, 4085-4093.
- 21 Z. Li, S. Liu, L. Li, W. Qi, W. Lai, L. Li, X. Zhao, Y. Zhang and W. Zhang, Sol. Energy Mater. Sol. Cells, 2021, 220, 110859.
- 22 C. Sun, J. Yang, Z. Dai, X. Wang, Y. Zhang, L. Li, P. Chen, W. Huang and X. Dong, Nano Res., 2016, 9, 1300-1309.
- 23 L. Zhao, M. Yang, Z. Zhang, Y. Ji, Y. Teng, Y. Feng and X. Liu, Inorg. Chem. Commun., 2018, 89, 22-26.
- 24 J. A. A. Mehrez, K. A. Owusu, Q. Chen, L. Li, K. Hamwi, W. Luo and L. Mai, Inorg. Chem. Front., 2019, 6, 857-865.
- 25 L. Wang, Y. Min, D. Xu, F. Yu, W. Zhou and A. Cuschieri, Chem. Commun., 2014, 50, 11147-11150.

**Paper** NJC

- 26 Y. C. Yang, Y. T. Wang and W. L. Tseng, ACS Appl. Mater. Interfaces, 2017, 9, 10069-10077.
- 27 Z. Chen, J. J. Yin, Y. T. Zhou, Y. Zhang, L. Song, M. Song, S. Hu and N. Gu, ACS Nano, 2012, 6, 4001-4012.
- 28 J. Mu, Y. Wang, M. Zhao and L. Zhang, Chem. Commun., 2012, 48, 2540-2542.
- 29 W. Chen, J. Chen, Y. Bin Feng, L. Hong, Q. Y. Chen, L. F. Wu, X. H. Lin and X. H. Xia, Analyst, 2012, 137, 1706-1712.
- 30 S. Fu, S. Wang, X. Zhang, A. Qi, Z. Liu, X. Yu, C. Chen and L. Li, Colloids Surf., B, 2017, 154, 239-245.
- 31 M. Gao, X. Lu, M. Chi, S. Chen and C. Wang, Inorg. Chem. Front., 2017, 4, 1862-1869.
- 32 Y. Ma, M. Zhu, Q. He, M. Zhao and H. Cui, ACS Sustainable Chem. Eng., 2022, 10, 5651-5658.
- 33 L. Zhang, P. Hu, X. Zhao, R. Tian, R. Zou and D. Xia, J. Mater. Chem., 2011, 21, 18279-18283.
- 34 G. Gao, H. B. Wu, S. Ding and X. W. Lou, Small, 2015, 11, 432-436.
- 35 S. Kandula and P. Jeevanandam, Eur. J. Inorg. Chem., 2015, 4260-4274.
- 36 W. Stober, A. Fink and E. Bohn, J. Colloid Interface Sci., 1968, 26, 62-69.
- 37 P. Yang, F. Wang, X. Luo, Y. Zhang, J. Guo, W. Shi and C. Wang, ACS Appl. Mater. Interfaces, 2014, 6, 12581-12587.
- 38 J. Xu, J. Liu, R. Che, C. Liang, M. Cao, Y. Li and Z. Liu, Nanoscale, 2014, 6, 5782-5790.
- 39 L. Kumar, H. Chauhan, N. Yadav, N. Yadav, S. A. Hashmi and S. Deka, ACS Appl. Energy Mater., 2018, 1, 6999-7006.
- 40 S. Liu, S. C. Lee, U. Patil, I. Shackery, S. Kang, K. Zhang, J. H. Park, K. Y. Chung and S. Chan Jun, J. Mater. Chem. A, 2017, 5, 1043-1049.
- 41 J. Yan, Z. Fan, W. Sun, G. Ning, T. Wei, Q. Zhang, R. Zhang, L. Zhi and F. Wei, Adv. Funct. Mater., 2012, 22, 2632-2641.
- 42 N. Y. Tashkandi and R. M. Mohamed, Ceram. Int., 2022, 48, 13216-13228.
- 43 P. Prieto, J. F. Marco, A. Serrano, M. Manso and J. de la Figuera, J. Alloys Compd., 2019, 810, 151912.
- 44 J. Mahajan and P. Jeevanandam, Mater. Today Commun., 2021, 26, 102085.
- 45 S. Wang, Y. Hou and X. Wang, ACS Appl. Mater. Interfaces, 2015, 7, 4327-4335.

- 46 R. Huang, J. Lin, J. Zhou, E. Fan, X. Zhang, R. Chen, F. Wu and L. Li, Small, 2021, 17, 1-9.
- 47 F. M. M. Borges, D. M. A. Melo, M. S. A. Câmara, A. E. Martinelli, J. M. Soares, J. H. de Araújo and F. A. O. Cabral, J. Magn. Magn. Mater., 2006, 302, 273-277.
- 48 S. K. Yadav and P. Jeevanandam, J. Nanoparticle Res., 2016, **18**, 1–25.
- 49 M. Iacob, D. Sirbu, C. Tugui, G. Stiubianu, L. Sacarescu, V. Cozan, A. Zeleňáková, E. Čižmár, A. Feher and M. Cazacu, RSC Adv., 2015, 5, 62563-62570.
- 50 T. H. Dolla, K. Pruessner, D. G. Billing, C. Sheppard, A. Prinsloo and P. Ndungu, Mater. Today Proc., 2018, 5, 10488-10495.
- 51 P. Pramanik, S. Thota, S. Singh, D. C. Joshi, B. Weise, A. Waske and M. S. Seehra, J. Phys.: Condens. Matter, 2017, 29, 425803.
- 52 Y. He, N. Li, W. Li, X. Zhang, X. Zhang, Z. Liu and Q. Liu, Sens. Actuators, B, 2021, 326, 128850.
- 53 X. Zhao, S. Zhao, S. Li, X. Yao, X. Zhu, W. Chen, G. Fan, Z. Liu, Q. Liu and K. Yue, ACS Appl. Nano Mater., 2021, 4, 8706-8715.
- 54 E. Ding, J. Hai, F. Chen and B. Wang, ACS Appl. Nano Mater., 2018, 1, 4156-4163.
- 55 X. Q. Zhang, S. W. Gong, Y. Zhang, T. Yang, C. Y. Wang and N. Gu, J. Mater. Chem., 2010, 20, 5110-5116.
- 56 X. Liu, Q. Wang, H. Zhao, L. Zhang, Y. Su and Y. Lv, Analyst, 2012, 137, 4552-4558.
- 57 J. Dong, L. Song, J. J. Yin, W. He, Y. Wu, N. Gu and Y. Zhang, ACS Appl. Mater. Interfaces, 2014, 6, 1959-1970.
- 58 Y. Zhu, Z. Yang, M. Chi, M. Li, C. Wang and X. Lu, Talanta, 2018, 181, 431-439.
- 59 W. Yang, J. Li, M. Wang, X. Sun, Y. Liu, J. Yang and D. H. L. Ng, Colloids Surf., B, 2020, 188, 110742.
- 60 L. Artiglia, S. Agnoli, M. C. Paganini, M. Cattelan and G. Granozzi, ACS Appl. Mater. Interfaces, 2014, 6, 20130-20136.
- 61 J. Mu, L. Zhang, G. Zhao and Y. Wang, Phys. Chem. Chem. Phys., 2014, 16, 15709-15716.
- 62 L. Huang, K. Chen, W. Zhang, W. Zhu, X. Liu, J. Wang, R. Wang, N. Hu, Y. Suo and J. Wang, Sens. Actuators, B, 2018, **269**, 79-87.
- 63 W. Huang, T. Lin, Y. Cao, X. Lai, J. Peng and J. Tu, Sensors, 2017, 17, 217-228.